Characterization of Oxidation Mechanisms in a Family of Polycrystalline Chromia-Forming Nickel-Base Superalloys

M.T. Lapington[1*], D.J. Crudden[2], R.C. Reed[1,2], M.P. Moody[1], P.A.J. Bagot[1]

[1]*Department of Materials, University of Oxford, Parks Road, Oxford OX1 3PH, UK*

5   [2]*Department of Engineering Science, University of Oxford, Parks Road, Oxford OX1 3PJ, UK*

ABSTRACT

The oxidation properties of a family of novel polycrystalline Ni-based superalloys with varying Ti:Nb ratio have been studied, which has shown a correlation between increasing

10   titanium content and accelerated oxidation kinetics. High-resolution characterization of microstructure and chemistry was carried out on the resultant oxide layers using SEM/EDX and Atom Probe Tomography to precisely locate Ti segregation within chromia scales, in order to identify a potential mechanism to explain this correlation. Despite some spread in the data, levels of Ti dissolved in the chromia oxide scales showed little correlation with the

15   nominal Ti concentration or the oxidation properties of each alloy, indicating that oxidation rates are not reliant on dopant levels within bulk chromia. A number of grain boundaries within the oxide scale were targeted for APT analysis, as these are known to act as short-circuit diffusion paths. Segregation of Ti, Nb and Ta to oxide grain boundaries was observed, suggesting that ion transport rates may instead be mediated by dopants present at grain

20   boundaries rather than dissolved within the bulk.

[*]**Corresponding Author:** Tel: +44 7956 940935   **Email:** mark.lapington@eng.ox.ac.uk

Present Address: Department of Engineering Science, Parks Rd, Oxford OX1 3PJ, UK

1.   INTRODUCTION

In order to withstand the demanding conditions experienced at the heart of modern jet turbine engines, nickel based superalloys must be optimized to combine properties with competing requirements during the alloy design stage. Resistance to temperature-dependent degradation mechanisms such as oxidation and fatigue is increasingly becoming a priority, as operating temperatures continue to be pushed higher due to tighter fuel economy and emissions targets [1]. Higher temperature regimes have been shown to increase the kinetics of oxidation reactions, while also enabling oxidation-related fatigue processes for which the mechanisms are currently poorly understood [2–4].

To design the next generation of polycrystalline turbine disc alloys, the relationship between oxidation kinetics and alloy composition must be established. Previous studies on nickel based alloys have suggested a link between titanium concentration and increased oxidation rates [5–10], however the high chemical complexity of these alloys makes direct comparisons problematic. To further investigate this link between composition and kinetics, a family of superalloys have been created with identical manufacturing routes and compositions except for the systematic replacement of Ti with Nb [11]. These two elements were chosen for substitution as both partition to γ′ phase precipitates [12], where they impart strength at high temperatures by increasing anti-phase boundary energy [13]. Nb is also a frequently used addition to many in-service alloys which does not result in the same detrimental increase to oxidation rates [14], making it a prime substitution candidate. However, Nb has been previously shown to be detrimental to dwell fatigue performance [15,16], which limits full substitution of Ti.

2

The mechanism by which Ti exacerbates oxidation is a matter of ongoing research. Several previous studies into this behaviour have utilized energy-dispersive X-ray spectroscopy (EDX) [5–9,14,17,18] and electron-probe micro-analysis (EPMA) [10,19] to characterize the distribution of elements through oxide layers. Many of these studies have observed dissolution of Ti into chromia scales, combined with the formation of discrete TiO_2 particles at the oxide-air and oxide-metal interfaces. These phenomena have been linked to the observed titanium-oxidation relationship via two proposed mechanisms; The first involves increasing ion transport rates through the bulk chromia lattice via cation vacancy creation [5,10,20,21], and the second mechanism involves faster short-circuit ion diffusion along dislocations or grain boundaries [6,22–25].

To investigate the viability of these mechanisms, it is critically important to precisely locate where Ti and other potentially detrimental trace elements segregate to within the oxide layers. EDX analysis has been carried out to benchmark these alloys against results obtained from previous studies, and further high-resolution characterization has been performed using Atom Probe Tomography (APT). APT is a three dimensional analysis technique which is extremely well suited to study of sub-nanometre scale composition and microstructure, which has previously been used to study trace element segregation to oxidised fatigue crack tips [26–29] and grain boundaries in oxide scales [30–35].

2.   Experimental Procedure

2.1.   Material Composition and Processing

The nickel-based superalloy compositions examined in this study were selected using the Alloys-By-Design process [36]. It first identifies composition-property relationships from a

3

database containing the compositions and properties of several commercially-available superalloys using neural network analysis. These composition-property relationships are then used to narrow down the available composition space, based on the properties required from the alloy, with the assistance of computational thermodynamics. This method has been implemented to design a family of γ/γ' polycrystalline superalloys which balance mechanical properties with corrosion resistance, for production of turbine discs with a projected operating temperature of 800°C [37].

Alloy		Ni	Cr	Co	W	Al	Ti	Ta	Nb	C	B	Zr	Fe	Si
ABD-2	Target	49.2	18.7	18.2	0.9	8.0	4.1	0.6	0.0	0.13	0.08	0.04	-	-
	Measured	48.5	18.9	18.5	1.0	7.9	4.3	0.7	0.0	0.13	0.05	0.04	0.00	0.00
ABD-4	Target	49.3	18.7	18.2	0.9	8.0	3.6	0.6	0.4	0.13	0.08	0.04	-	-
	Measured	48.5	18.6	18.6	0.9	7.9	4.0	0.6	0.4	0.14	0.10	0.04	0.00	0.04
ABD-5	Target	49.3	18.7	18.2	0.9	8.0	3.2	0.6	0.8	0.13	0.08	0.04	-	-
	Measured	49.4	18.6	18.3	0.9	7.6	3.3	0.6	0.8	0.14	0.11	0.04	0.03	0.06
ABD-6	Target	49.3	18.7	18.2	0.9	8.0	2.8	0.6	1.2	0.13	0.08	0.04	-	-
	Measured	48.1	18.9	18.8	0.9	8.1	2.9	0.6	1.2	0.12	0.11	0.04	0.03	0.06

Table 1 – Target and measured compositions (at.%) of ABD series superalloys investigated in this study [12]. Composition measurements were made using multiple spectroscopy techniques, including: X-ray fluorescence, combustion infra-red method and inductively coupled plasma-optical emission.

Nominal compositions for the four alloys are shown in Table 1, together with as-manufactured compositions measured using a combination of spectroscopy techniques including x-ray fluorescence (XRF), combustion infra-red method and inductively coupled plasma optical emission spectroscopy (ICP-OES). These alloys have also previously

undergone APT characterization, which has verified the bulk chemistry as well as phase

90 chemistries and elemental partitioning coefficients [12].

The alloys were created by ATI powder metals using a lab-scale version of their commercial

powder metallurgy processing route, consisting of powder production, compaction via hot

isostatic pressing (HIP), and isothermal forging into pancake forgings. A two-stage heat

95 treatment was then carried out consisting of γ' phase solutionizing at 1170°C (30°C above

the predicted γ' solvus temperature) for 2 hours, followed by aging at 850°C (50°C above the

projected operation temperature) for 4 hours.

2.2. Thermo-Gravimetric Analysis (TGA)

100 The isothermal oxidation properties and kinetics of these alloys were evaluated using a

Netszch Jupiter F1 TGA, in which the mass gain due to oxide growth was measured over 100

hours at the projected operating temperature of 800°C. Samples of 10mm^2 cross-sectional

area and 1mm thickness were polished to a 1200 grit finish using successively finer grades of

SiC grit paper, then ultrasonically cleaned in an isopropyl alcohol bath. Initial sample masses

105 were measured using a microbalance with 10μg resolution, and total surface areas were

calculated via micrometre. Samples were then suspended within the vertical tube furnace

using platinum wire, which was enclosed within a sheath of argon gas to prevent

atmospheric contamination. The experiment consisted of 3 sections: temperature ramp up

to 800°C at 50°C/s in Ar gas to prevent early oxidation, isothermal hold at 800°C in synthetic

110 dry lab air (80% N_2, 20% O_2 mix) for 100 hours, followed by ramp down to room

temperature in Ar at 50°C/s. A background run with no loaded sample was carried out to

calibrate for buoyancy effects resulting from temperature and internal atmosphere density

changes. Initial data analysis was carried out in the Netszch Proteus software suite. After

TGA analysis the oxidized samples were bisected using a Buehler Isomet low speed saw,

115 with one half mounted to an SEM stub using conductive silver epoxy for FIB

characterization, and the other prepared for cross-sectional analyses by cold mounting in

high-viscosity low-shrinkage epoxy resin.

2.3. Energy Dispersive X-ray Spectroscopy (EDX)

120 Mounted samples were analysed using a Zeiss Merlin SEM fitted with an Oxford Instruments

Xmax 150 EDX detector. Sample preparation involved grinding to a mirror polish using

successively finer grades of SiC grit paper and diamond suspension, followed by $0.06\mu m$

COL-K colloidal silica. Thin strips of silver dag were applied to the finished surface to avoid

image drift caused by sample charging from the electron beam. FIB cross-sections

125 underwent EDX analysis using a Zeiss Crossbeam 540 fitted with an Oxford Instruments

XmaxN 150 EDX detector. The oxide surface was protected with a deposited platinum layer,

followed by trenching and polishing using a 30kV 300pA Ga ion beam. For both instruments,

a 10keV beam current was selected to give high-resolution images while activating enough

principal emission lines to avoid major peak overlaps, particularly the overlap between the

130 Cr Lα and O Kα lines around 0.55 keV. All EDX micrographs and spectroscopic data were

analysed in the Oxford Instruments Aztec 3.3 nanoanalysis software suite.

2.4. Focussed Ion Beam - Scanning Electron Microscopy (FIB-SEM)

FIB-SEM is a technique for analysing material cross-sections at specific sites without

135 requiring coating or mounting, thereby limiting any obstruction of microstructural features

6

or sample contamination. A Zeiss Nvision 40 dual beam FIB-SEM was used to cut trenches through the oxide layers by focusing a 30kV Ga ion beam with a current of 3nA, reducing down to 700pA at the trench edges to limit Ga ion damage. The exposed cross-sectional surface was polished using a rastered 30kV, 300pA beam to give a smooth surface while minimising the beam curtaining effects that often result from density variations within the oxide layer. During FIB milling, the surface was kept under constant observation with the SEM column at 5kV accelerating voltage using a 120μm aperture. As the cross-section is not perpendicular to the SEM column, a 36° tilt correction was applied to the resultant micrographs. Final micrographs were obtained using both the SE2 detector to record surface features, and the Inlens detector for increased phase contrast.

2.5. FIB Liftout Procedure

After locating a potential site to lift out during FIB cross-sectioning, a protective layer of tungsten was deposited over a 30μm x 3μm area to prevent Ga ion or e$^-$ beam damage to the underlying oxide. A series of trenches were cut at a 30° angle to the surface to remove material beneath the protected region and create a liftout bar. A Kleindiek micromanipulator was used to extract the liftout and 'weld' sections using tungsten onto a silicon micropost array in order to create individual atom probe tips. A 700pA rastered Ga ion beam separated each liftout section, which underwent several annular milling steps to thin each tip down to a sub-100nm tip diameter. These steps began using a 30kV, 300pA ion beam, slowly reducing down to 30kV, 150pA as the tips approached 500μm width, followed by a final polishing step consisting of a 5kV, 250pA imaging mill. The sample was oriented so that the full microstructural cross-section could be viewed throughout all of these steps, and

micrographs were captured so that depth estimates of the final tip below the surface could

160 be made.

2.6.   Atom Probe Tomography (APT)

APT analysis of the specimens was undertaken in laser-pulsing mode with a low pulse

frequency to increase yield and prevent fractures in the fragile and poorly conducting

165 oxides. A Cameca LEAP 3000X HR was used to characterise samples of alloy ABD-4, using a

532nm wavelength green laser with pulse energy of 0.4nJ and pulse frequency of 160MHz at

a stage temperature of 50K. A Cameca LEAP 5000XR was used to perform all other APT

analyses, using a 355nm wavelength UV laser with pulse energy of 50pJ at a stage

temperature of 50K. For the LEAP 5000XR, a variable laser pulse rate was used to maximize

170 ion yield without compromising on observable mass-to-charge-state ratio range (with an

upper range limit set to 250Da). All APT data were reconstructed and analysed using

Cameca IVAS 3.8.0 software, with additional mass spectrum analyses carried out using the

freely-accessible APTtools [38,39] and AtomProbeLab [40] software suites.

175 # 3.   RESULTS

3.1.   Oxidation Kinetics

The oxidation properties of the four ABD-series alloys were evaluated at 800°C by

measuring the change in specific mass (mass change per unit area) over 100 hours. Mass

gain data underwent a background correction to account for buoyancy effects caused by

180 changes in temperature and gas composition. All alloys displayed specific mass gain rates

8

following a parabolic growth law, in agreement with the Wagner theory of diffusion-controlled oxidation [41,42]. The parabolic rate constant K_p has been determined using:

$$(\Delta m)^n = K_p t \qquad \text{Eq. 1}$$

Where Δm is the specific mass change (kg.m^{-2}), t is exposure time (s), and K_p is the parabolic rate constant (kg^{2}m^{-4}s^{-1}). A power law exponent of n=2 has been assumed based on the parabolic behaviour of previously obtained data captured at 800°C [6,43]. Specific mass gain squared has been plotted against time in Figure 1, with K_p values determined from the gradient of the linear fit. Some deviation from linearity can be seen for all alloys present in this graph, but most prominently for the high-Ti alloy ABD-2 (4.1Ti, 0Nb). It is unknown whether these deviations are caused by mass loss events such as oxide spallation, changes in kinetics such as transient phase formation, or buoyancy changes related to air pressure/temperature.
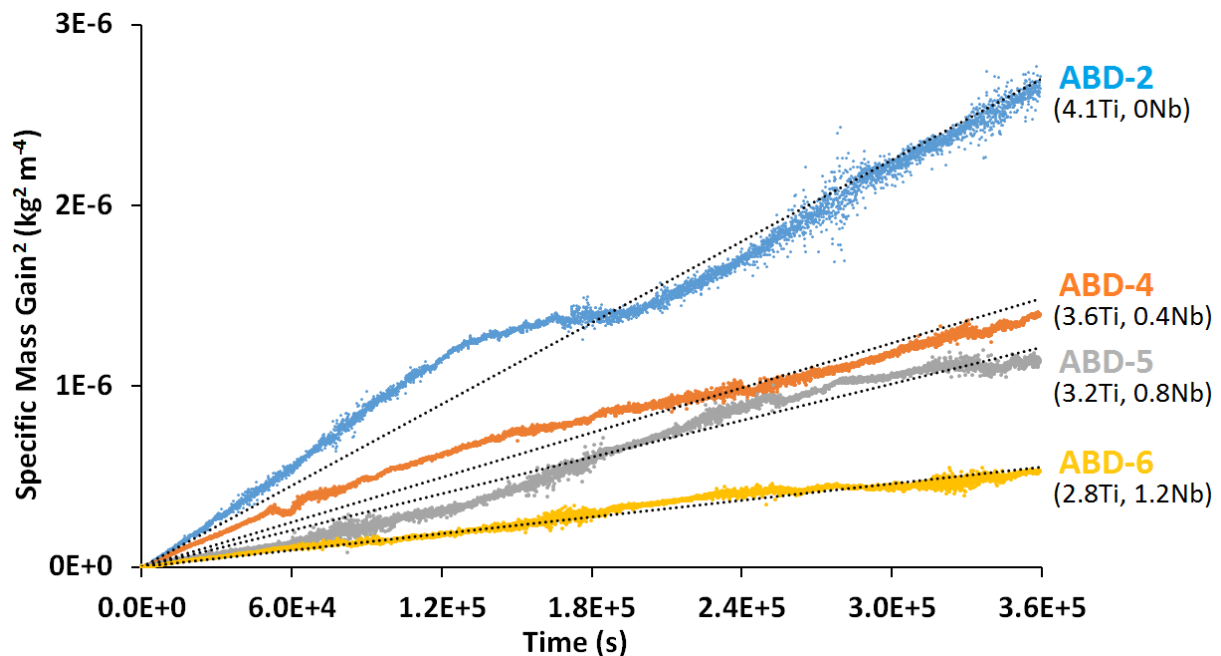

Figure 1 – Thermo-gravimetric analysis plot of specific mass gain squared over time, used to determine parabolic rate constant (K_p).

Despite these deviations the oxidation kinetics can still be compared between the alloys, which shows a clear correlation between higher Ti concentration (in at.%) and increasing oxidation rates. Measured K_p values (in units of $kg^2m^{-4}s^{-1}$) range from a maximum of 7.5 x10^{-12} for the high-Ti alloy ABD-2 (4.1Ti, 0Nb), down to 1.5 x10^{-12} for the low-Ti alloy ABD-6 (2.8Ti, 1.2Nb). This range of K_p values is comparable to values obtained between 750°C and 850°C in a variety of other nickel based superalloys [6,7,9,18,43–45]. Measurements of specific mass gain can be used as an indicator of the adverse effect of increasing Ti concentration on oxidation kinetics, but they do not take into account the type and depth of oxidation attack, which are also important metrics for accurately estimating fatigue lifetime.
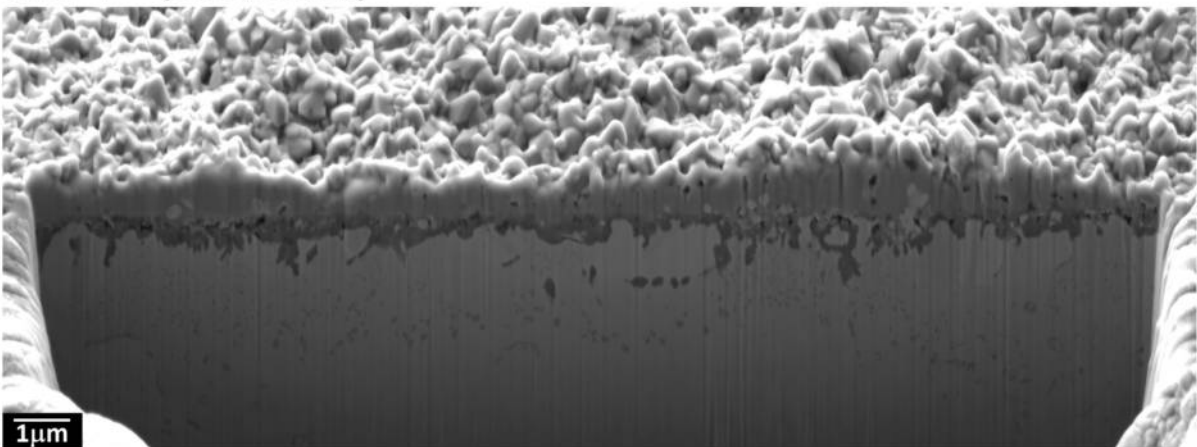
3.2.   Cross-Sectional Analyses

The chromia-forming nickel based superalloys investigated in this study oxidize in the same manner as Group II superalloys as described by Giggins and Pettit [46]. This designation is given to alloys which form a protective external chromia (Cr_2O_3) scale, as well as internal alumina (Al_2O_3) in the form of either a continuous subscale or individual islands.

The morphology and chemistry of oxide scales can vary significantly with small changes in alloy composition, so two different forms of cross-sectional analysis were carried out to assess this. To study oxide morphology, multiple FIB-SEM cross sections through oxide scales were analysed from remote areas of samples from each alloy, of which three representative cross sections are shown in Figure 2. These micrographs were taken from the Nb-free alloy ABD-2 (4.1Ti, 0Nb), the low-Nb alloy ABD-4 (3.6Ti, 0.4Nb), and the high-Nb alloy ABD-6 (2.8Ti, 1.2Nb).
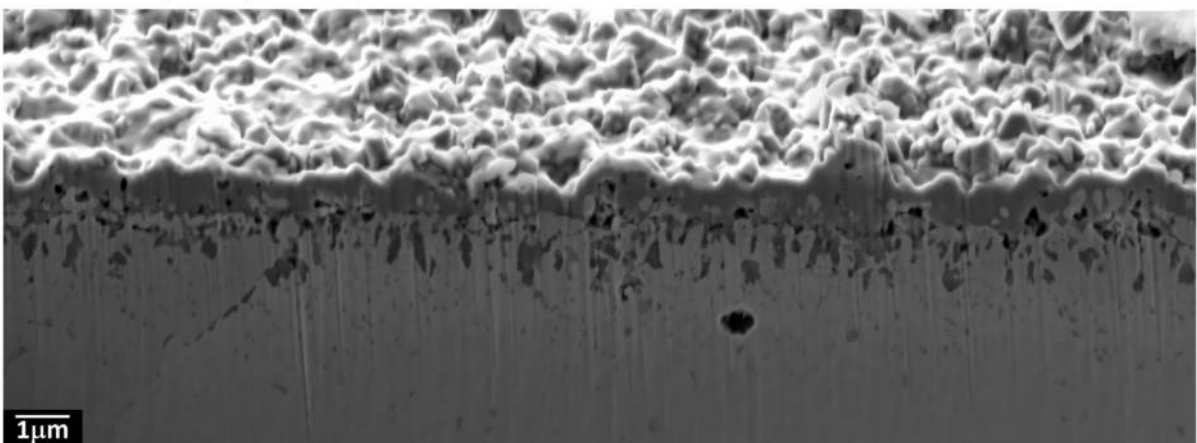
Figure 2 – 5kX magnification FIB-SEM cross sections through oxide scales from the Nb-free alloy ABD-2 (4.1Ti, 0Nb), the low-Nb alloy ABD-4 (3.6Ti, 0.4Nb), and the high-Nb alloy ABD-6 (2.8Ti, 1.2Nb).

225 The major alumina and chromia layers can be distinguished from one another using FIB-SEM by their differing contrast, but to locate other elements and identify smaller oxide regions EDX spectroscopy was utilised as shown in Figure 3. Both methods confirm that all of the ABD alloys studied here comprise layers of external chromia and internal alumina oxide scales, which is the expected ordering derived from an Ellingham diagram as the partial

230 pressure of oxygen decreases as a function of depth below the surface [47]. Areas of unoxidized γ phase matrix can be seen trapped between oxide layers in all samples shown. EDX maps also show a region of Cr and Al depletion in the γ matrix directly below the scale.

Some variation in distribution and morphology can be seen, with the Nb-containing alloys

235 tending to exhibit uniform continuous chromia scales and discontinuous but evenly distributed internal alumina islands. In contrast, the Nb-free alloy ABD-2 displayed continuous chromia of varying thickness including pronounced ridges formed above areas of increased internal oxidation, combined with deep alumina intrusions following certain grain boundaries several microns into the matrix.

240

EDX analysis corroborated all of the features characterised by SEM, and also helped to identify a number of Ti-rich particles occurring at the oxide-air interface, most likely in the form of rutile TiO_2 which has been reported previously in the literature [6,7,9,48]. Nb seems to be absent from the oxide layer and is only detected in appreciable quantities in the γ

245 matrix. In addition some Nb signal was detected from the protective Pt capping layer, which is likely caused by a peak overlap between the Nb Lα and Pt M emission lines around 2.1keV.
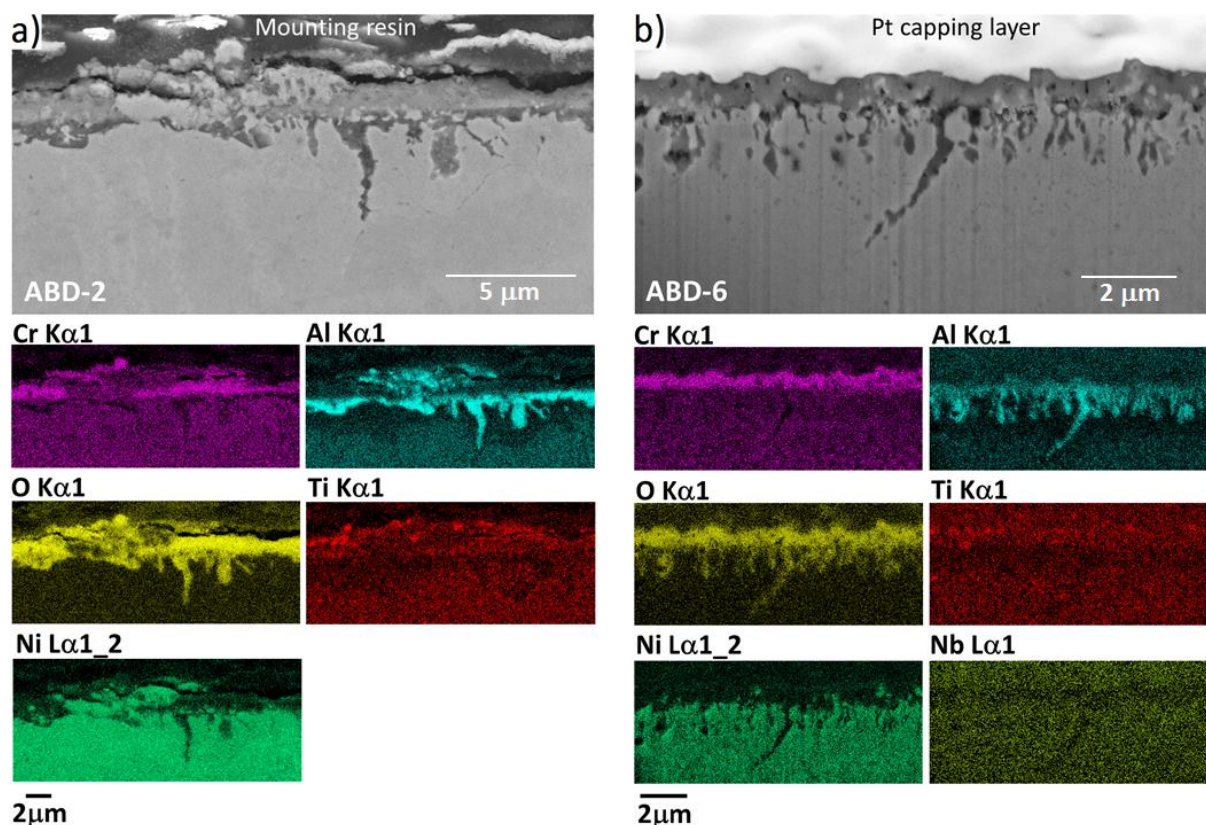
Figure 3 – 5kX magnifications of SEM cross-sectional micrographs and individual EDX element maps obtained at 10kV for the high-Ti alloy ABD-2 (4.1Ti, 0Nb) and the low-Ti alloy ABD-6 (2.8Ti, 1.2Nb).

3.3.   Chromia Composition APT Analysis

In order to examine the elemental distributions and microstructure at the sub-nanometre scale, APT was carried out on samples obtained from site-specific FIB liftouts, which were carefully prepared from a range of depths through the oxide scale. A total of 23 successful atom probe tips from within the oxide layers were reconstructed and analysed, from which 12 reconstructions consisting only of chromia with minimal grain boundaries or other large phases present were analysed to determine chromia compositions across the alloys. These reconstructions varied in size from 12 million to 164 million ions, and the resultant mass-to-charge-state ratio spectra incorporated between 87 to 135 individual peaks. Accurate composition determination requires careful identification of these peaks. Hence, the

13

association of specific ionic species to mass spectrum peaks was undertaken systematically in a particular order, with frequent cross-checking with the APTtools software suite [38]. Many of the peaks contained contributions from multiple ionic species with overlapping mass-to-charge-state ratio values. The relative contributions of the different types of ions to an overlapping peak was estimated using a deconvolution algorithm based on the assumption of natural isotopic abundances and adjacent non-overlapping peaks [49]. This is a probabilistic technique that allows composition measurement accuracy to be maintained, but cannot definitively determine the spatial distribution of the component ionic species. Fortunately, this is not a problem when determining average bulk compositions.
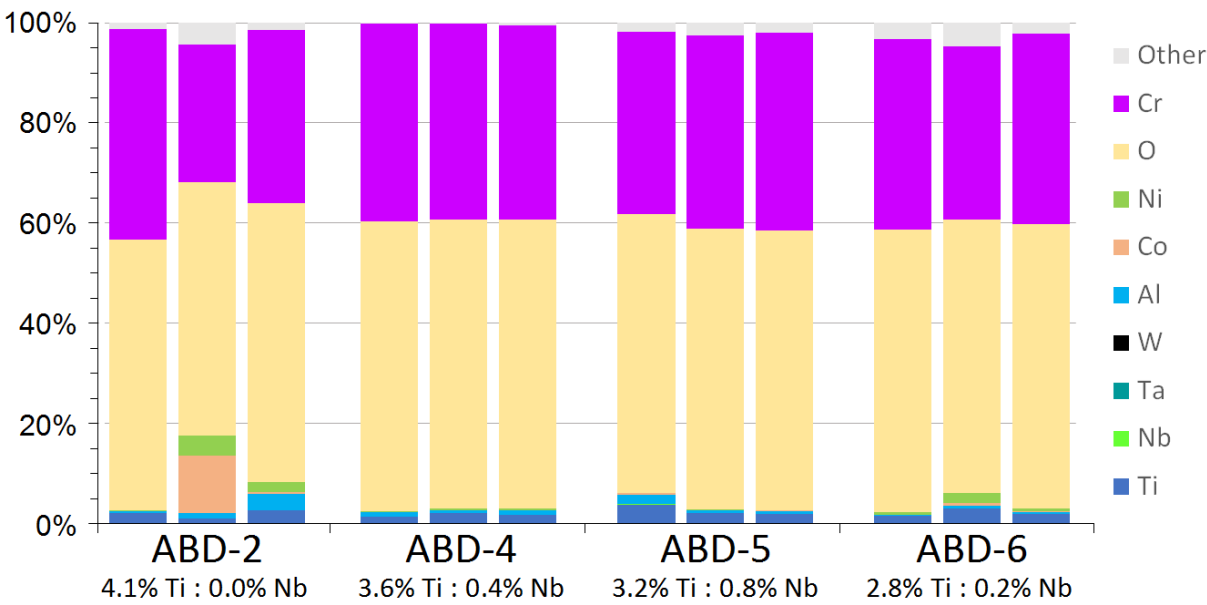
After the mass spectra were ranged, APT reconstructions were further analysed to identify any precipitates, retained matrix or other non-chromia phases. Many small NiCo-rich retained γ phase particles were identified as well as two NiTi-rich particles. All were removed from the chromia composition analysis by isolating and extracting them using a 5at.% Ni iso-concentration surface. Final chromia compositions were calculated by re-applying the deconvolution algorithm for the mass spectra associated to these localised regions of the data to address the peak overlaps, followed by decomposing all complex ionic species into their component elements. The r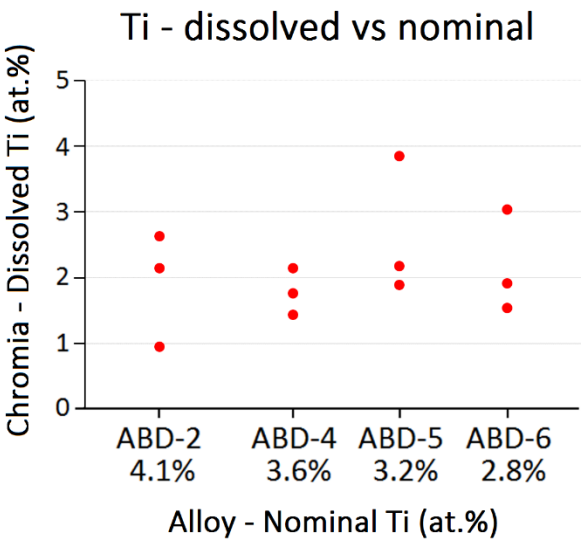esultant dataset compositions are shown in Figure 4. The majority of chromia datasets were found to consist mostly of stoichiometric Cr_2O_3, with the addition of between 2% and 22% elemental impurities. As Ti concentration is of particular interest, it has been displayed at the bottom of the stacked bar graph, so that each Ti concentration shares a common baseline. The amount of dissolved Ti in these chromia reconstructions varies from 1% to 4%, showing little correlation to the nominal Ti% in the alloy, as shown in Figure 5. It must be noted that the small number of samples and

14

significant scatter in the data means caution must be advised when drawing conclusions based on this data alone.

Figure 4 – Deconvoluted chromia compositions for 12 APT reconstructions across all four ABD alloys.

Figure 5 – Nominal alloy Ti concentrations (in at.%) as measured by ICP-OES, compared against dissolved Ti (in at.%) measured in chromia using APT.

3.4. Site-Specific APT Analysis

Many of the site-specific liftout specimens contained microstructural features with high concentrations of locally-segregated elements, such as grain boundaries within the chromia layer, regions of Cr-depleted γ matrix, and TiN particles enriched in Nb and Cr. These features made the datasets unsuitable for determining average chromia compositions. The three-dimensional nature of atom probe datasets allows these complex features to be studied with more microstructural context than projection-based analysis methods, however care must be taken when trying to ascertain the spatial distribution of ions in overlapping peaks. The total number of counts from each of these overlapping ions can be derived by using a deconvolution algorithm, but the spatial distributions of these ions cannot be separated from one another so easily. In the APT reconstructions that follow, peaks in the associated mass spectra have simply been identified as the most abundant ionic species contributing to that peak.
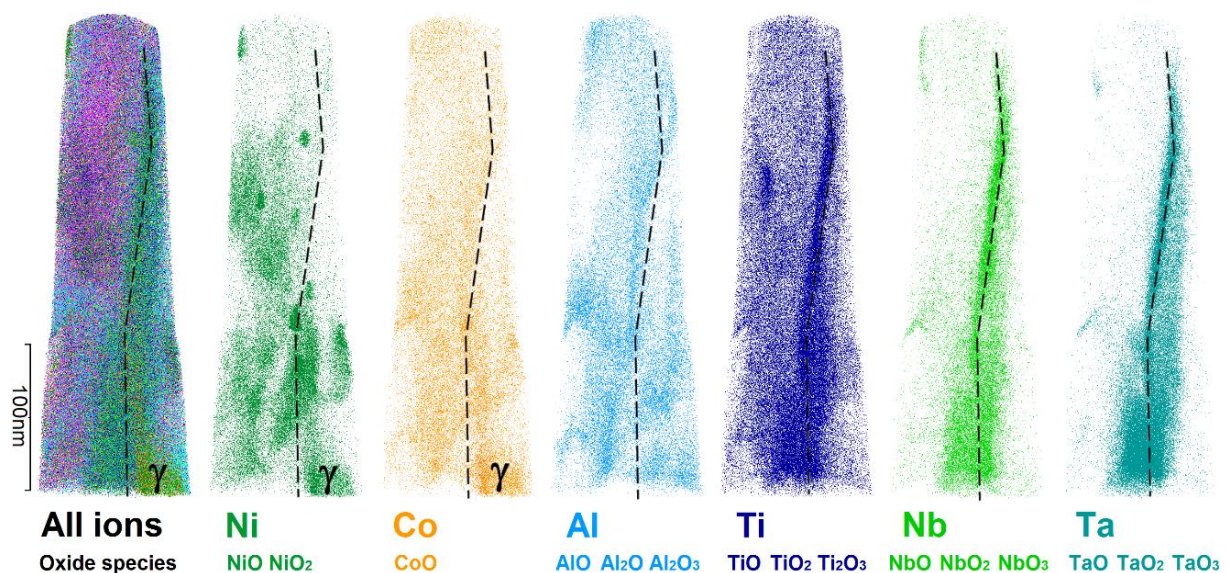

Figure 6 – Atom maps of an oxide grain boundary (represented by the dotted line) in the high-Nb ABD-6 alloy (2.8Ti, 1.2Nb), separated into individual maps showing a selection of elements and their associated oxide species.

16

Figure 6 shows a representative atom map from a chromia sample created from the high-Nb

ABD-6 alloy (2.8Ti, 1.2Nb), with each element, and detected molecular oxide species

containing that element, presented individually to highlight segregation behaviour. Cr and

Cr-containing ionic species have been excluded as they are distributed uniformly throughout

the sample. A grain boundary can be seen edge-on (represented by the dotted line in Figure

6), showing enrichment of Ti, Nb and Ta to the interface. A small region of NiCo-rich

retained γ phase was observed at the bottom of the feature, and some discrete Ni-rich

nodules were also observed on the 10-20nm scale.

Grain boundary enrichment of stable oxide forming elements was observed across multiple

datasets. Figure 7 presents an APT reconstruction of surface oxide from the Nb-free ABD-2

alloy (4.1Ti, 0Nb) which contains a grain boundary. This data has been further analysed by

creating a 60nm x 10nm x 10nm region of interest perpendicular to the grain boundary and

calculating a 1D concentration profile along it using the AtomProbeLab software suite [40].

Currently, this is the only software capable of peak deconvolution of the data as it is

sampled along 1D concentration profiles. This capability is critical for separating the various

overlaps between Ti- and O-containing species such as Ti_{48}^{3+}/O_{16}^{+} at 16Da and

$Ti_{48}O_{16}^{2+}/O_{16}O_{16}^{+}$ at 32Da. These overlaps are a particular concern at grain boundaries,

where the change in electric field required to evaporate ions could potentially cause a

change in ionic charge state ratios [34,50], in particular an increase in O_2^{+} at 32Da. This can

lead to an artificial increase in observed peak heights, which could be misconstrued as

evidence of grain boundary segregation despite it being a field-induced artefact.
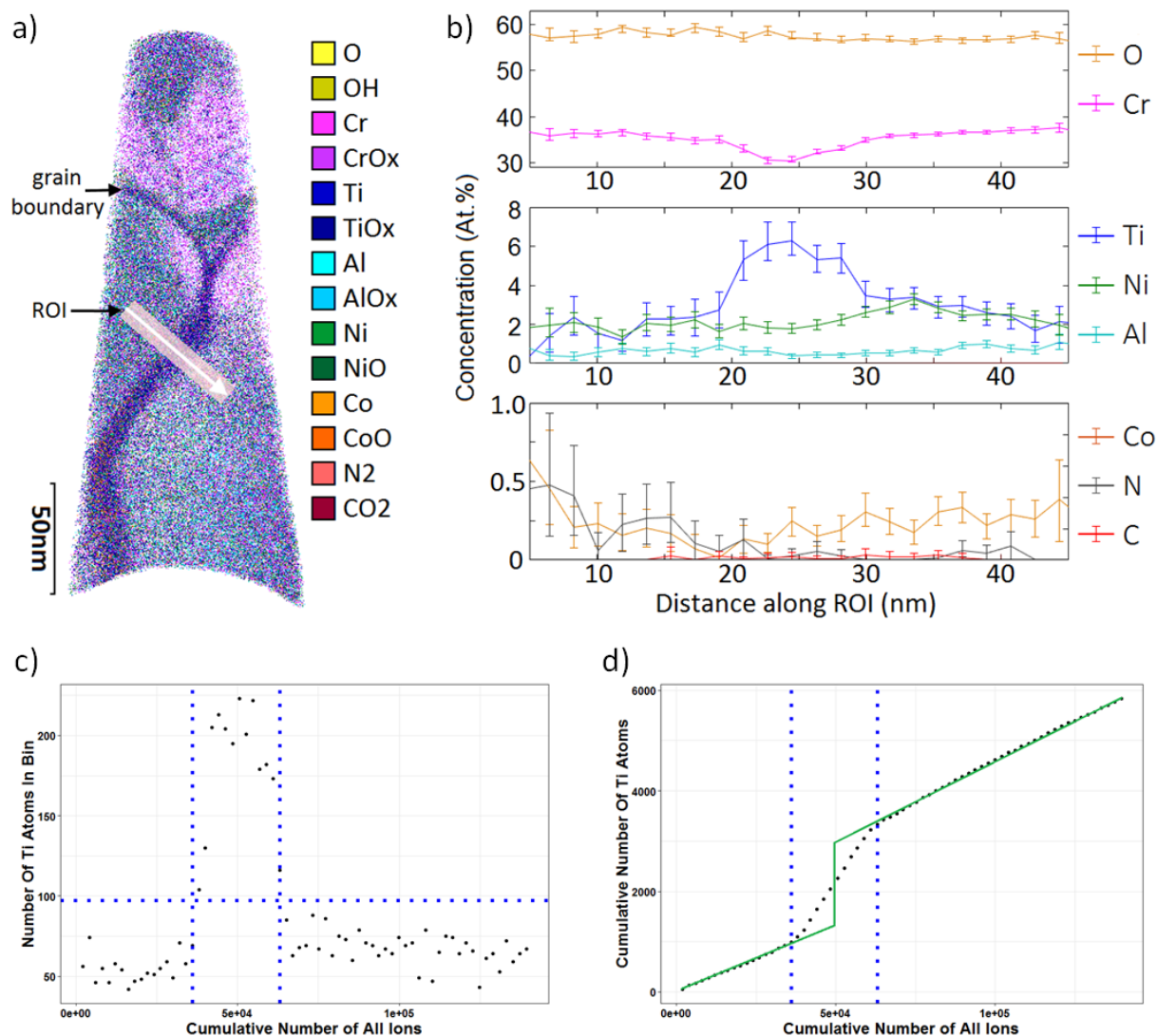
Figure 7 – a) A 10nm slice through a reconstruction of alloy ABD-2 (4.1Ti, 0Nb), containing a highly-segregated grain boundary. b) Deconvoluted 1D concentration profiles across a grain boundary shows segregation of Ti at the expense of Cr. c) 1D distribution of Ti over grain boundary, used to calculate: d) Cumulative Ti profile, extrapolated to a 2D interface to calculate Gibbsian Excess values.

Use of deconvoluted concentration profiles provides further confidence that the measured segregation of Ti, at the expense of Cr, is in fact genuine. A Gibbsian interfacial excess value for Ti of 18 atoms.nm^{-2} was calculated at this interface using a custom R script written by

Dr. Ben Jenkins, using the methodology shown in Figure 7 parts c) and d). No segregation data for Nb, Ta or W could be obtained as no peaks relating to these elements were detected in this dataset. The chromia also varies in composition, as indicated by the colour change in the map, with the lighter region in the upper section of the dataset consisting of near-stoichiometric chromia and the darker blue region showing enrichment of Ti, Ni, and Al (with concentrations of 3.2at.%, 2.5at.% and 0.9at.% respectively).

A similar analysis approach was carried out on the APT reconstruction of the low-Ti, high-Nb alloy ABD-6 (2.8Ti, 1.2Nb) as shown in Figure 8. Here all Cr-containing species have been removed to better present the local segregation of Nb, Al, and Ti-containing ionic species. This allows the nanocrystalline oxide grain structure to be seen, as well as a large NiCo-rich retained γ particle surrounded by a layer of Ni, Co, and Nb oxides. Local segregation of Nb to oxide grain boundaries is clearly visible, although Gibbsian interfacial excess values were difficult to determine due to the low concentrations involved. In this case, the segregation behaviour of Ti is much more subtle. The atom maps shown in Figure 8 a) and initial 1D concentration profiles obtained using the IVAS software indicated a small amount of grain boundary Ti segregation, however this was no longer apparent after repeating the analysis using AtomProbeLab software which accounted for the peak overlaps in the mass spectra. This indicates that field-induced evaporation of O_2^+ is likely occurring here rather than Ti segregation. Within the oxide grains Ti often co-segregates with Ni, which can be seen in Figure 8 as small blue particles adjacent to the grain boundaries.
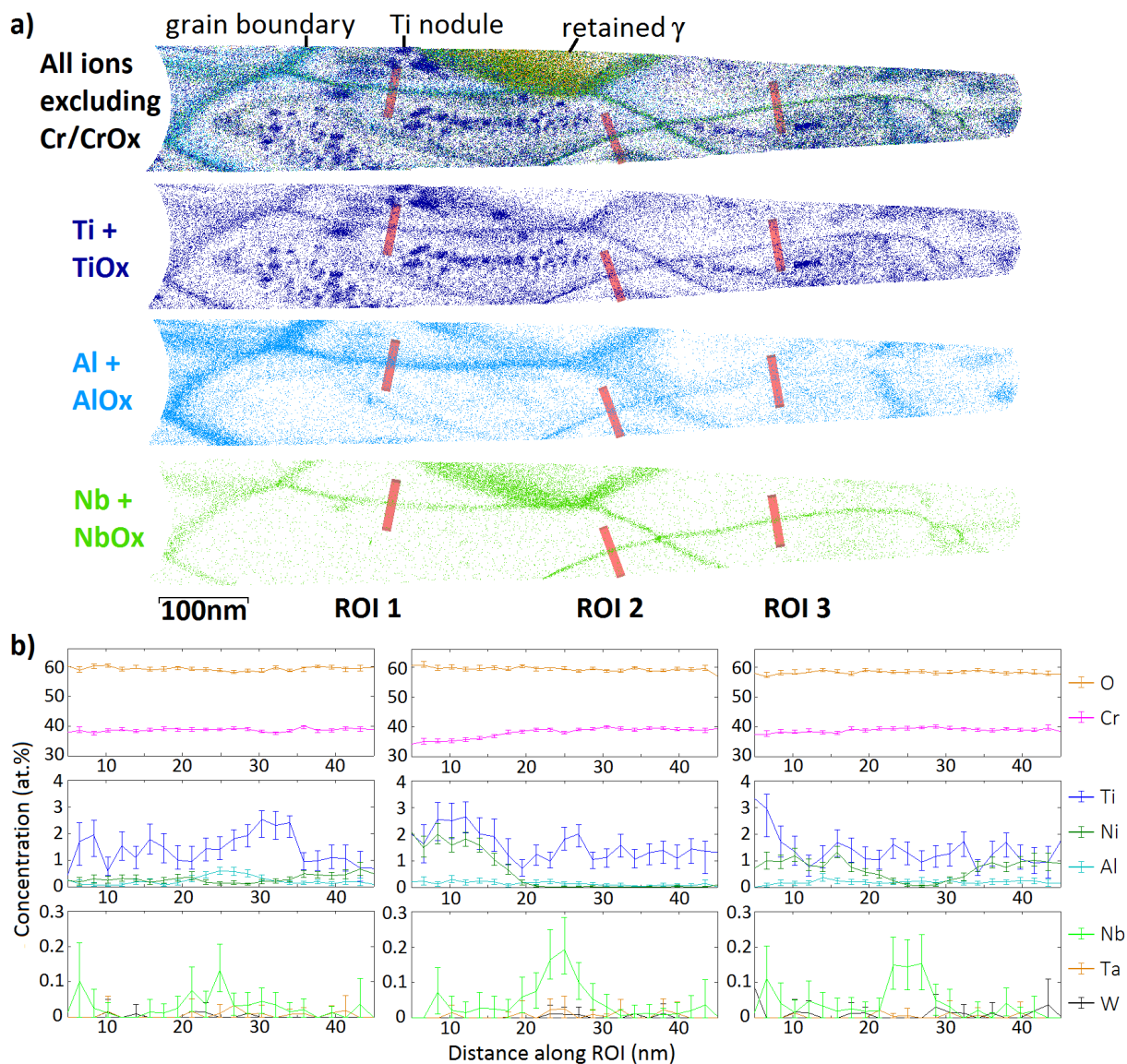
Figure 8 – a) A 10nm slice through chromia reconstruction of alloy ABD-6 (2.8Ti, 1.2Nb), with Cr-containing species removed to better show segregation. b) Deconvoluted 1D concentration profiles across multiple ROIs created over oxide grain boundaries.

370

Three additional datasets were also obtained from the deepest depth within the oxide layer, which intersects the alumina-metal interface. One of these datasets obtained from the high-Nb ABD-6 alloy (2.8Ti, 1.2Nb) is shown in Figure 9, as well as a number of isoconcentration surfaces used to define phase boundaries and a region of interest created across the alumina-metal interface. The chemistry across the alumina-matrix phase boundary was

375

analysed using a set of 1-dimensional concentration profiles. For clarity, these have been

separated into high and low-concentration decomposed element distributions, as well as

non-decomposed ionic distributions for a selection of oxide species. A 10nm thick oxide

region rich in Nb, Ni, Ta, and Co oxides can be seen lying directly at the alumina/gamma
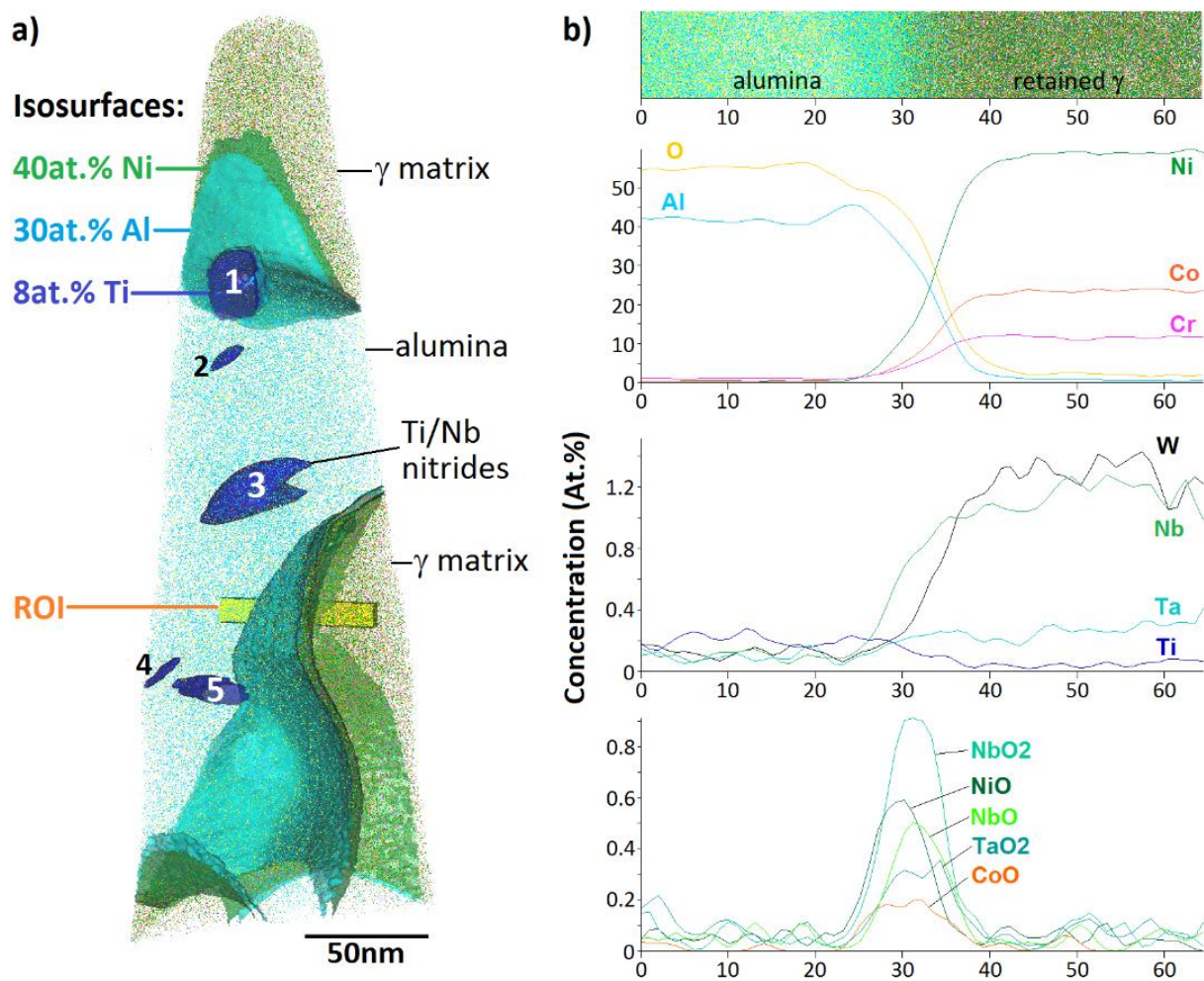
interface.

Figure 9 – a) Reconstruction of an alumina-metal interface from alloy ABD-6 (2.8Ti, 1.2Nb) including isosurfaces used to determine phase compositions. b) A region of interest created over the alumina-metal interface showing elemental distributions and oxides at the interface.

21

A phase composition analysis of the phases present is also shown in Table 2, which includes both regions of retained γ matrix extracted using a 40at.% Ni isoconcentration surface, the

390 alumina extracted using a 30at.% Al isosurface, and a number of TiN particles extracted using an 8at.% Ti isosurface. This reveals near-stoichiometric alumina, a chromium-depleted matrix, and a number of near-stoichiometric TiN particles enriched with Nb and Cr. The presence of Al and O within these nitrides results from a shell of Al_2O_3 remaining after extraction, most likely due to ion trajectory overlaps. Eight of these nitride particles were

395 found across the two ABD-6 (2.8Ti, 1.2Nb) alumina/metal interface reconstructions, with none observed in the high-Ti ABD-4 (3.6Ti, 0.4Nb) alumina/metal interface reconstruction.

	Ion Count	Al	B	C	Co	Cr	N	Nb	Ni	O	Ta	Ti	W
Retained γ	23,977,358	1.97	0.00	0.02	23.37	12.39	0.15	1.23	55.96	3.20	0.21	0.54	0.97
Alumina	52,935,252	43.61	0.01	0.02	0.86	0.72	0.15	0.07	0.56	53.23	0.01	0.74	0.01
Nitride AVG	692,922	6.72	0.01	0.30	0.14	2.34	19.92	4.81	11.20	21.91	0.41	32.10	0.14
Nitride 1	165,697	10.09	0.00	0.29	-	1.82	33.22	2.73	0.18	14.96	0.13	35.40	-
Nitride 2	21,404	13.45	0.01	0.20	-	1.61	29.36	3.57	0.15	19.82	0.12	30.62	-
Nitride 3	406,245	11.11	0.00	0.20	-	1.61	32.31	4.35	0.14	15.56	0.09	33.30	-
Nitride 4	33,941	14.20	0.01	0.24	-	2.86	25.86	4.09	0.18	24.00	0.25	26.92	-
Nitride 5	66,220	12.08	0.00	0.25	-	4.34	28.85	3.86	0.30	19.20	0.26	29.28	-

Table 2 – Phase compositions (in at.%) from reconstruction of alloy ABD-6 (2.8Ti, 1.2Nb) as

400 shown in Figure 9. Phases determined using shown isosurfaces. Individual nitride particles extracted using 8at.% Ti isosurface and re-ranged for composition analysis.

4. DISCUSSION

4.1. Compositional Effects on Oxide Morphology

405 The most obvious external sign of the change in oxidation properties between the alloys can be seen in the SEM and EDX cross-sectional micrographs of Figures 2 and 3. These figures

show that the oxide scales formed on the Nb-containing alloys ABD-4 (3.6Ti, 0.4Nb) and

ABD-6 (2.8Ti, 1.2Nb) are comprised of a uniform continuous outer chromia layer with

evenly-dispersed internal alumina islands, while the Nb-free alloy ABD-2 (4.1Ti, 0Nb) grows

410   a more irregular external chromia scale, often above deep internal alumina intrusions along

grain boundaries. As the alloys and oxidation conditions were designed to remove as many

external variables as possible, this change in oxide morphology is likely attributed to the

varying Ti:Nb ratio. Addition of Ti has been linked to irregular oxide formation in Alloy 617

and Haynes 230 by Kim et al. [8], as well as the formation of thick oxide ridges above grain

415   boundaries by Chen et al. [7], Taylor et al. [9] and Cruchley et al. [6] in a number of

commercially-available nickel superalloys. Grain boundaries are known to act as short-circuit

diffusion paths, so the thickening of oxide ridges above them in the higher-Ti alloys indicates

that grain boundary ion transport rates are composition-dependent, although whether this

is solely due to a change in Ti or Nb concentration is unknown. The addition of Nb has been

420   previously shown by Weng et al. [14] to smoothen the morphology of oxide scales in a

family of model alloys, which appears to correlate with the micrographs shown in Figure 2

where both Nb-containing alloys show a more consistent outer chromia layer. However the

alloys in that study contain significantly less Ti and more Nb, both at 2.0at.%.

425   This composition-dependent morphology has a number of implications, perhaps the most

relevant of which for industrial applications is that oxidation kinetics alone may not be an

adequate indicator for determining oxidation damage, as grain boundary intrusions have

been shown to act as potential fatigue crack initiation sites. Cruchley et al. [6], and Karabela

et al. [17] have previously arrived at similar conclusions with respect to oxidation damage.

430   One potential upside of these deep alumina intrusions has been presented by Whittle et al.

[51], which theorise that these intrusions can act as 'keys' to help prevent oxide spallation and maintain scale integrity.

The formation and characterization of subscale TiN particles enriched in Nb and Cr is also noteworthy. Their location beneath the alumina scale, where the oxygen partial pressure is low, is expected as nitride formation requires a reducing environment [7]. Taylor et al. [9] and Chen et al. [7] have also observed subsurface titanium nitrides, however the APT analyses carried out in this work in Figure 9 and Table 2 show the complexities in their shape and composition apparent when utilising high-resolution APT characterisation.

4.2. Relationship between Composition and Kinetics

Oxidation kinetics have been found to vary with composition as measured by thermo-gravimetric analysis (TGA), which supports previous studies investigating the role of increasing titanium concentration on oxidation kinetics [7,8,10]. Figure 1 shows that the mass gain due to oxide growth follows a parabolic path, which according to Wagner et al. [41] implies that the rate-limiting step for oxide growth is ion diffusion through a continually thickening scale. It is likely that these two phenomena are connected, with Ti concentration directly affecting rates of ion diffusion through the scale.

Chromia is known to be a p-type semiconductor at high oxygen partial pressures ($P_{O2} > 10^{-5}$ atm) [52], where the main charge carriers are electron holes and chromium vacancies. One of the more frequently cited mechanisms for creating chromium vacancies was originally proposed by Callister et al [53] by way of a high-valence cation doping mechanism. This involves the creation of cation vacancies during TiO_2 dissolution in Cr_2O_3, where the

24

aliovalent substitution of 4 Cr^{3+} ions with 3 Ti^{4+} ions on Cr lattice sites requires the creation of an additional cation vacancy in order to maintain charge neutrality, as shown in Equation 2 [20] :

$$3TiO_2 \rightarrow 3Ti_{Cr}^{\bullet} + V_{Cr}''' + 6O_O \qquad \text{Eq. 2}$$

where $Ti_{Cr}^{\bullet}$ is a Ti atom with one effective positive charge on a Cr lattice site, and V_{cr}''' is a cation vacancy with three effective negative charges. It is these additional cation vacancies which are implicated in the increased rates of cation diffusion through chromia.

Experiments by Atkinson et al. [20] and Blacklocks et al. [21] have verified this cation vacancy mechanism in pure α-chromia doped with Ti by utilizing X-ray diffraction (XRD), density and electrical conductivity measurements combined with computer simulation of defect energies. This mechanism has also been investigated in more complex superalloys, such as in experiments performed on INCOLOY 800H by Grübmeier et al. [19] involving XRD and X-ray Absorption Spectroscopy (XAS). These have also shown Ti^{4+} ions and vacancies to be located within the bulk chromia lattice, however, this lattice diffusion mechanism alone cannot explain the increase in oxidation kinetics displayed by these alloys, as the Ti concentration dissolved in the chromia as measured by APT showed little correlation with the nominal alloy Ti concentrations (Figure 5) nor their associated kinetics (Figure 1). This implies that the mechanism does not solely depend on defect density in the bulk lattice. One interesting potential mechanism that fits with the observations in this study involves an increase in cation diffusion out of the metal along oxide grain boundaries, which helps to explain the variation in oxide morphology displayed in Figure 2.

4.3. Impact of Ti Segregation on Potential Mechanisms

Segregation of Ti to oxide grain boundaries has been previously characterised using atom probe tomography in a number of material/oxide systems. This behaviour has been seen in nickel superalloys by Pedrazzini et al. [35] in chromia scales formed on alloy RR1000, and by Jeong et al. [54] in chromia scales formed on Alloy 617. Grain boundary Ti segregation has also been observed in steels by Povstugar et al. [34] in alumina scales formed on ODS-strengthened MA956, and by Vayyala et al. [31] in chromia scales formed on Fe-Cr-Mn ferritic steels. Every one of these studies has noted that grain boundaries act as short-circuit diffusion pathways, especially in nanocrystalline materials with a high grain boundary cross-section to volume ratio. This is explicitly addressed by Pedrazzini et al. [35], who performed diffusion simulations which suggest that grain boundaries are likely to form the main outward cation diffusion path.

Manipulation of grain boundary diffusion characteristics via deliberate addition of certain reactive elements is a well-established field of research, known as the Reactive Element Effect [51,55–58]. Many superalloys already incorporate elements such as Y, Hf, La and Zr in order to preferentially segregate to oxide grain boundaries, where they improve scale adhesion by acting as sulfur-getters, and also reduce oxidation rates by inhibiting cation transport [59]. Ti repeatedly appears as an outlier in this regard, as it has been shown to segregate to chromia grain boundaries and accelerate oxidation rather than inhibit it. During this study Nb has also been observed segregating to oxide grain boundaries (as seen in Figure 8) without any associated increase to oxidation rates (as seen in Figure 1). This is despite having a higher valency than Ti, as shown by Vayyala et al. [31] who observed the presence of Nb segregation at chromia grain boundaries in the form of Nb^{4+} or Nb^{5+} ions.

The observations presented in this paper have focussed on alloys with varying Ti:Nb ratio, so any conclusions regarding the effects of Ti or Nb addition cannot easily be separated. It follows that either the disproportionate oxidation-accelerating effect of Ti grain boundary segregation is caused by some property other than its high valency (such as its relatively high solubility in chromia), or that Nb segregation to grain boundaries somehow inhibits cation transport in a similar manner to the Reactive Element Effect.

Also, from the bulk and grain boundary composition data presented in this study it is reasonable to conclude that ion transport rates through oxides formed on these alloys are determined by grain boundary ion diffusion rather than bulk lattice diffusion via the creation of cation vacancies. This helps to explain why Ti segregated to grain boundaries can have such an effect on the oxidation kinetics, while also explaining the increasing size of alumina intrusions and grain boundary ridges due to increased anion flow into the metal.

SUMMARY & CONCLUSIONS

- Thermo-Gravimetric Analyses (TGA) was performed on a series of alloys with varying Ti:Nb ratio, which resulted in parabolic oxidation rate curves indicating that the oxidation kinetics are based on ion diffusion through the oxide scale. Oxidation rates also correlate well with Ti:Nb ratio.
- Cross-sectional electron microscopy techniques verified that the oxide scale exists as a dual-layer of external chromia above an internal alumina subscale, as predicted based on consideration of oxygen partial pressure as a function of depth from the surface. A composition dependence was also observed, with the Nb-free alloy ABD-2 (4.1Ti, 0Nb) exhibiting rough, irregular chromia above deep alumina grain boundary intrusions, whereas the Nb-containing alloys ABD-4 (3.6Ti, 0.4Nb) and ABD-6 (2.8Ti, 1.2Nb) exhibited smooth external chromia and evenly-distributed internal alumina islands.

27

- Atom Probe Tomography was used to obtain compositions of the chromia scales from all ABD alloys in the present study, revealing near-stoichiometric Cr_2O_3 with additions of up to 22at.% impurities consisting mostly of Ti, Ni and Al. Despite some spread in the data, it does not appear that the Ti concentration dissolved in chromia scales correlates with the nominal alloy Ti concentration, and by extension the oxidation kinetics.

- APT reconstructions of grain boundaries within chromia layers were obtained. 1D concentration profiles across these boundaries, that account for peak overlaps in the associated mass spectra, show high levels of segregation from Ti and Nb.

- APT analysis of the alumina-metal interface revealed near-stoichiometric alumina, Cr-depleted matrix phase, as well as near-stoichiometric TiN nitrides enriched with Nb and Cr.

- As the Ti concentration dissolved in chromia does not appear to correlate with the displayed oxidation kinetics, and large amounts of Ti were observed segregated to grain boundaries, grain boundary diffusion was determined to be the rate-defining mechanism for the oxidation of ABD-series alloys at 800°C over the time period of 100 hours.

REFERENCES

[1] P. Busquin, P. Argüelles, M. Bischoff, B.A.C. Droste, S. Evans, W. Kröll, J.-L. Lagardère, A. Lina, J. Lumsden, D. Ranque, S. Rasmussen, P. Reutlinger, S. Robins, H. Terho, A. Wittlöw, European aeronautics: a vision for 2020 — a synopsis, Air Sp. Eur. 3 (2001) 16–18. https://doi.org/10.1016/S1290-0958(01)90042-5.

[2] K.S. Chan, A Grain Boundary Fracture Model for Predicting Dynamic Embrittlement and Oxidation-Induced Cracking in Superalloys, Metall. Mater. Trans. A Phys. Metall. Mater. Sci. 46 (2015) 2491–2505. https://doi.org/10.1007/s11661-015-2860-1.

[3] E. Andrieu, R. Molins, H. Ghonem, A. Pineau, Intergranular crack tip oxidation mechanism in a nickel-based superalloy, Mater. Sci. Eng. A. 154 (1992) 21–28. https://doi.org/10.1016/0921-5093(92)90358-8.

[4] R. Jiang, D. Proprentner, M. Callisti, B. Shollock, X.T. Hu, Y.D. Song, P.A.S. Reed, Role of oxygen in enhanced fatigue cracking in a PM Ni-based superalloy: Stress assisted grain boundary oxidation or dynamic embrittlement?, Corros. Sci. (2018). https://doi.org/10.1016/j.corsci.2018.05.001.

[5] H. Buscail, S. Perrier, C. Josse, Oxidation mechanism of the Inconel 601 alloy at high temperatures, Mater. Corros. 62 (2011) 416–422. https://doi.org/10.1002/maco.200905519.

[6] S. Cruchley, H.E. Evans, M.P. Taylor, M.C. Hardy, S. Stekovic, Chromia layer growth on a Ni-based superalloy: Sub-parabolic kinetics and the role of titanium, Corros. Sci. 75 (2013) 58–66. https://doi.org/10.1016/j.corsci.2013.05.016.

[7] J.H. Chen, P.M. Rogers, J.A. Little, Oxidation behavior of several chromia-forming commercial nickel-base superalloys, Oxid. Met. 47 (1997) 381–410. https://doi.org/10.1007/BF02134783.

[8] D. Kim, C. Jang, W.S. Ryu, Oxidation characteristics and oxide layer evolution of Alloy 617 and Haynes 230 at 900 °C and 1100 °C, Oxid. Met. 71 (2009) 271–293. https://doi.org/10.1007/s11085-009-9142-5.

[9] M.P. Taylor, H.E. Evans, S. Stekovic, M.C. Hardy, The oxidation characteristics of the nickel-based superalloy, RR1000, at temperatures of 700 - 900°C, Mater. High Temp. 29 (2012) 145–150. https://doi.org/10.3184/096034012X13341417107382.

[10] H. Nagai, M. Okabayashi, Deleterious Effect of Ti Addition on the Oxidation Resistance of Ni-20Cr Alloy, Trans. Japan Inst. Met. 22 (1981) 691–698. https://doi.org/10.2320/matertrans1960.22.691.

[11] R. Reed, D. Crudden, B. Raeisinia, M.C. Hardy, Nickel based alloy composition, European Patent Office EP2894234, 2015. https://data.epo.org/gpi/EP2894234B1.

[12] M.T. Lapington, D.J. Crudden, R.C. Reed, M.P. Moody, P.A.J. Bagot, Characterization of phase chemistry and partitioning in a family of high-strength nickel-based superalloys, Metall. Mater. Trans. A. 49 (2018) 2302–2310. https://doi.org/10.1007/s11661-018-4558-7.

[13] D.J. Crudden, A. Mottura, N. Warnken, B. Raeisinia, R.C. Reed, Modelling of the influence of alloy composition on flow stress in high-strength nickel-based superalloys, Acta Mater. 75 (2014) 356–370. https://doi.org/10.1016/j.actamat.2014.04.075.

[14] F. Weng, H. Yu, C. Chen, K. Wan, High-temperature oxidation behavior of Ni-based superalloys with Nb and Y and the interface characteristics of oxidation scales, Surf. Interface Anal. 47 (2015) 362–370. https://doi.org/10.1002/sia.5718.

[15] X.J. Pang, D.J. Dwyer, M. Gao, P. Valerio, R.P. Wei, Surface enrichment and grain boundary segregation of niobium in Inconel 718 single-and poly-crystals, Scr. Metall. Mater. 31 (1994) 345–350. https://doi.org/10.1016/0956-716X(94)90294-1.

[16] L.G. Zhao, J. Tong, M.C. Hardy, Prediction of crack growth in a nickel-based superalloy under fatigue-oxidation conditions, Eng. Fract. Mech. 77 (2010) 925–938. https://doi.org/10.1016/j.engfracmech.2010.02.005.

[17] A. Karabela, L.G. Zhao, J. Tong, N.J. Simms, J.R. Nicholls, M.C. Hardy, Effects of cyclic stress and temperature on oxidation damage of a nickel-based superalloy, Mater. Sci. Eng. A. 528 (2011) 6194–6202. https://doi.org/10.1016/j.msea.2011.04.029.

[18] S. Seal, S. Kuiry, L. Bracho, Studies on the surface chemistry of oxide films formed on IN-738LC superalloy at elevated temperatures in dry air, Oxid. Met. 56 (2001) 583–603. https://doi.org/10.1023/a:1012569803467.

[19] H.B. Grübmeier, A. Naoumidis, H.A. Schulze, Titanium distribution in multilayer oxide scales on oxidized INCOLOY 800H, J. Vac. Sci. Technol. A Vacuum, Surfaces, Film. 4 (1986) 2565–2570. https://doi.org/10.1116/1.573728.

[20] A. Atkinson, M.R. Levy, S. Roche, R.A. Rudkin, Defect properties of Ti-doped Cr_2O_3, Solid State Ionics. 177 (2006) 1767–1770. https://doi.org/10.1016/j.ssi.2005.11.015.

[21] A. Blacklocks, A. Atkinson, R. Packer, S. Savin, A. Chadwick, An XAS study of the defect structure of Ti-doped α-Cr2O3, Solid State Ionics. 177 (2006) 2939–2944. https://doi.org/10.1016/j.ssi.2006.08.028.

[22] B.A. Pint, J.R. DiStefano, I.G. Wright, Oxidation resistance: One barrier to moving beyond Ni-base superalloys, Mater. Sci. Eng. A. 415 (2006) 255–263. https://doi.org/10.1016/j.msea.2005.09.091.

[23] S.B. Newcomb, W.M. Stobbs, The effects of a grain boundary on the compositional fluctuations inherent in the oxidation of Fe-10Cr-34Ni, Oxid. Met. 35 (1991) 69–88. https://doi.org/10.1007/BF00666501.

[24] W.D. Kingery, H.K. Bowen, D.R. Uhlmann, Introduction to ceramics, John wiley & sons, 1976.

[25] D.J. Young, High temperature oxidation and corrosion of metals, Elsevier, 2008.

[26] K. Kruska, S. Lozano-Perez, D.W. Saxey, T. Terachi, T. Yamada, G.D.W. Smith, Nanoscale characterisation of grain boundary oxidation in cold-worked stainless steels, Corros. Sci. 63 (2012) 225–233. https://doi.org/10.1016/j.corsci.2012.06.030.

[27] L. Viskari, M. Hörnqvist, K.L. Moore, Y. Cao, K. Stiller, Intergranular crack tip oxidation in a Ni-base superalloy, Acta Mater. 61 (2013) 3630–3639. https://doi.org/10.1016/j.actamat.2013.02.050.

[28] H.S. Kitaguchi, M.P. Moody, H.Y. Li, H.E. Evans, M.C. Hardy, S. Lozano-Perez, An atom probe tomography study of the oxide–metal interface of an oxide intrusion ahead of a crack in a polycrystalline Ni-based superalloy, Scr. Mater. 97 (2015) 41–44. https://doi.org/10.1016/j.scriptamat.2014.10.025.

[29] A. La Fontaine, H.W. Yen, P.J. Felfer, S.P. Ringer, J.M. Cairney, Atom probe study of chromium oxide spinels formed during intergranular corrosion, Scr. Mater. 99 (2015) 1–4. https://doi.org/10.1016/j.scriptamat.2014.09.028.

[30] P. Kontis, S. Pedrazzini, Y. Gong, P.N. Bagot, M.P. Moody, R.C. Reed, The effect of boron on oxide scale formation in a new polycrystalline superalloy, Scr. Mater. 127 (2017) 156–159. https://doi.org/10.1016/j.scriptamat.2016.09.013.

[31] A. Vayyala, I. Povstugar, D. Naumenko, W.J. Quadakkers, H. Hattendorf, J. Mayer, A Nanoscale Study of Thermally Grown Chromia on High-Cr Ferritic Steels and Associated Oxidation Mechanisms, J. Electrochem. Soc. 167 (2020) 061502. https://doi.org/10.1149/1945-7111/ab7d2e.

[32] D.J. Young, T.D. Nguyen, P. Felfer, J. Zhang, J.M. Cairney, Penetration of protective chromia scales by carbon, Scr. Mater. 77 (2014) 29–32. https://doi.org/10.1016/j.scriptamat.2014.01.009.

[33] T.D. Nguyen, A. La Fontaine, L. Yang, J.M. Cairney, J. Zhang, D.J. Young, Atom probe study of impurity segregation at grain boundaries in chromia scales grown in CO2gas, Corros. Sci. 132 (2018) 125–135. https://doi.org/10.1016/j.corsci.2017.12.024.

[34] I. Povstugar, J. Weber, D. Naumenko, T. Huang, M. Klinkenberg, W.J. Quadakkers, Correlative atom probe tomography and transmission electron microscopy analysis of grain boundaries in thermally grown alumina scale, Microsc. Microanal. 25 (2019) 11–20. https://doi.org/10.1017/S143192761801557X.

[35] S. Pedrazzini, B.S. Rowlands, A. Turk, I.M.D. Parr, M.C. Hardy, P.A.J. Bagot, M.P. Moody, E. Galindo-Nava, H.J. Stone, Partitioning of Ti and Kinetic Growth Predictions on the Thermally Grown Chromia Scale of a Polycrystalline Nickel-Based Superalloy, Metall. Mater. Trans. A Phys. Metall. Mater. Sci. 50 (2019) 3024–3029. https://doi.org/10.1007/s11661-019-05246-5.

[36] R.C. Reed, T. Tao, N. Warnken, Alloys-By-Design: Application to nickel-based single crystal superalloys, Acta Mater. 57 (2009) 5898–5913. https://doi.org/10.1016/j.actamat.2009.08.018.

[37] D.J. Crudden, B. Raeisinia, N. Warnken, R.C. Reed, Analysis of the Chemistry of Ni-Base Turbine Disk Superalloys Using An Alloys-By-Design Modeling Approach, Metall. Mater. Trans. A. 44 (2012) 2418–2430. https://doi.org/10.1007/s11661-012-1569-7.

[38] D. Haley, APTtools, (2018). http://apttools.sourceforge.net/ (accessed April 8, 2019).

[39] D. Haley, P. Choi, D. Raabe, Guided mass spectrum labelling in atom probe tomography, Ultramicroscopy. 159 (2015) 338–345. https://doi.org/10.1016/j.ultramic.2015.03.005.

[40] A.J. London, AtomProbeLab, (2018). https://sourceforge.net/projects/atomprobelab/ (accessed April 8, 2019).

[41] C. Wagner, Theoretical Analysis of the Diffusion Processes Determining the Oxidation Rate of Alloys, J. Electrochem. Soc. 99 (1952) 369. https://doi.org/10.1149/1.2779605.

[42] N. Birks, G.H. Meier, Introduction to High Temperature Oxidation of Metals, E. Arnold, 1983.

[43] S. Cruchley, M.P. Taylor, H.E. Evans, P. Bowen, M.C. Hardy, S. Stekovic, Microstructural Characterisation of High Temperature Oxidation of Nickel Base Superalloy RR1000 and the Effect of Shot-Peening, Superalloys 2012 12th Int. Symp. Superalloys. (2012) 751–758. https://doi.org/10.1002/9781118516430.ch83.

[44]   A. Encinas-Oropesa, G.L. Drew, M.C. Hardy, A.J. Leggett, J.R. Nicholls, N.J. Simms, Effects of oxidation and hot corrosion in a nickel disc alloy, Superalloys 2008 11th Int. Symp. Superalloys. (2008) 609–618. https://doi.org/10.7449/2008/Superalloys_2008_609_618.

[45]   U. Krupp, W. Kane, J.A. Pfaendtner, L. Xinyu, C. Laird, C.J. McMahon Jr, Oxygen-Induced Intergranular Fracture of the Nickel-Base Alloy IN718 during Mechanical Loading at High Temperatures, Mater. Res. 7 (2004) 1–7. https://doi.org/10.1590/S1516-14392004000100006.

[46]   C.S. Giggins, F.S. Pettit, Oxidation of Ni-Cr-Al Alloys Between 1000° and 1200°C, J. Electrochem. Soc. 118 (1971) 1782. https://doi.org/10.1149/1.2407837.

[47]   C.W. Dannatt, H.J.T. Ellingham, Roasting and Reduction Processes – A General Survey, Discuss. Faraday Soc. (1948) 126–139. https://doi.org/10.1039/DF9480400126.

[48]   B.J. Foss, M.C. Hardy, D.J. Child, D.S. McPhail, B.A. Shollock, Oxidation of a Commercial Nickel-Based Superalloy under Static Loading, Jom. 66 (2014) 2516–2524. https://doi.org/10.1007/s11837-014-1196-4.

[49]   D.J. Larson, T.J. Prosa, R.M. Ulfig, B.P. Geiser, T.F. Kelly, Local Electrode Atom Probe Tomography, Springer New York, New York, NY, 2013. https://doi.org/10.1007/978-1-4614-8721-0.

[50]   B. Gault, M.P. Moody, J.M. Cairney, S.P. Ringer, Atom probe microscopy, Springer Science & Business Media, 2012.

[51]   D.P. Whittle, J. Stringer, Improvements in High Temperature Oxidation Resistance by Additions of Reactive Elements or Oxide Dispersions, Philos. Trans. R. Soc. A Math. Phys. Eng. Sci. 295 (1980) 309–329. https://doi.org/10.1098/rsta.1980.0124.

[52]   M.-Y. Su, G. Simkovich, Point Defect Structure of Chromium (III) Oxide, in: Non-Stoichiometric Compd., Springer Netherlands, Dordrecht, 1989: pp. 93–113. https://doi.org/10.1007/978-94-009-0943-4_7.

[53]   W.D. Callister, M.L. Johnson, I.B. Cutler, R.W. Ure, Sintering Chromium Oxide with the Aid of TiO2, J. Am. Ceram. Soc. 62 (1979) 208–211. https://doi.org/10.1111/j.1151-2916.1979.tb19056.x.

[54]   H. Jeong, S.H. Kim, W.S. Choi, P.P. Choi, Spallation resistance of oxide scales on Alloy 617 enhanced by boron addition, Corros. Sci. 140 (2018) 196–204. https://doi.org/10.1016/j.corsci.2018.06.002.

[55]   H. Nagai, M. Okabayashi, M. Hiroyasu, The Effects of Rare Earths and Reactive elements on the Oxidation Resistance on Ni-20Cr Alloy, Trans. Japan Inst. Met. 21 (1980). https://doi.org/10.2320/matertrans1960.21.341.

[56]   B.A. Pint, Experimental observations in support of the dynamic-segregation theory to explain the reactive-element effect, Oxid. Met. 45 (1996) 1–37. https://doi.org/10.1007/BF01046818.

[57]   B. Pieraggi, Chromia Scale Growth in Alloy Oxidation and the Reactive Element Effect, J. Electrochem. Soc. 140 (1993) 2844. https://doi.org/10.1149/1.2220920.

[58]   S. Chevalier, What did we learn on the reactive element effect in chromia scale since Pfeil's patent?, Mater. Corros. 65 (2014) 109–115. https://doi.org/10.1002/maco.201307310.

[59]   B.A. Pint, Progress in Understanding the Reactive Element Effect Since the Whittle and Stringer Literature Review, Proc. John Stringer Symp. High Temp. Corros. Mater. Park. Ohio ASM Int. (2003) 9–19.